RESEARCH ARTICLE | JUNE 26 2023

Achieving ultrahigh energy storage density in super relaxor BCZT-based lead-free capacitors through multiphase coexistence ⊘

Sun Zixiong (孙梓雄) ✉ ⓘ ; Yuhan Bai ⓘ ; Tao Ouyang ⓘ ; Qing Guo ⓘ ; Yating Ning; Jiaqi Liu ⓘ ; Hansong Wei; Kang Du; Hongmei Jing ✉ ; Ye Tian ⓘ ; Yongping Pu ✉ ⓘ
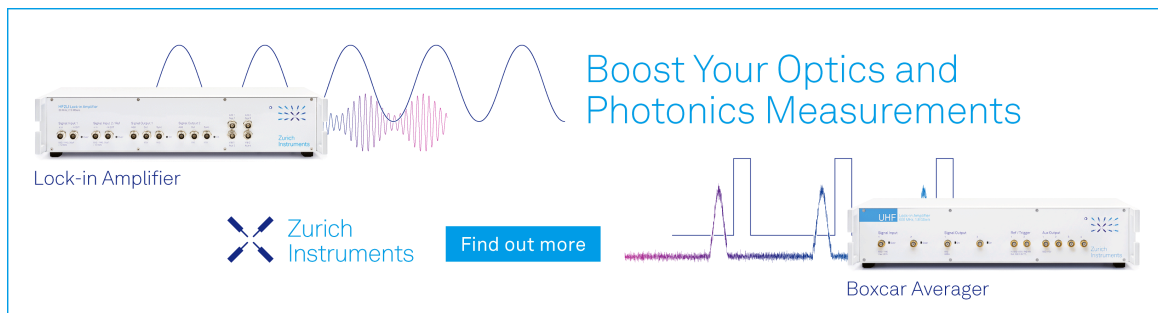
Check for updates

View Online

Export Citation

Achieving ultrahigh energy storage density in super relaxor BCZT-based lead-free capacitors through multiphase coexistence

Zixiong Sun (孙梓雄),[1,2,3,4,a] Yuhan Bai,[1] Tao Ouyang,[5] Qing Guo,[1] Yating Ning,[5] Jiaqi Liu,[6] Hansong Wei,[6] Kang Du,[7] Hongmei Jing,[8,a] Ye Tian,[9] and Yongping Pu[5,a]

AFFILIATIONS

[1] School of Electronic Information and Artificial Intelligence, Shaanxi University of Science and Technology, Xi'an 710021, People's Republic of China
[2] Key Laboratory of Auxiliary Chemistry and Technology for Chemical Industry, Ministry of Education, Shaanxi University of Science and Technology, Xi'an 710021, People's Republic of China
[3] Shaanxi Collaborative Innovation Center of Industrial Auxiliary Chemistry and Technology, Shaanxi University of Science and Technology, Xi'an 710021, China
[4] MESA+ Institute for Nanotechnology, University of Twente P.O. Box 217, 7522 NH Enschede, The Netherlands
[5] Shaanxi Key Laboratory of Green Preparation and Functionalization for Inorganic Materials, Shaanxi University of Science and Technology, Xi'an 710021, People's Republic of China
[6] Shaanxi Provincial Key Laboratory of Papermaking Technology and Specialty Paper Development, National Demonstration Center for Experimental Light Chemistry Engineering Education, Key Laboratory of Paper Based Functional Materials of China National Light Industry, Shaanxi University of Science and Technology, Xi'an 710021, People's Republic of China
[7] School of Mathematical and Physical Sciences, Wuhan Textile University, Wuhan 430200, China
[8] School of Physics and Information Technology, Shaanxi Normal University, Xi'an 710119, People's Republic of China
[9] School of Materials Science and Engineering, Shaanxi University of Science and Technology, Xi'an 710021, People's Republic of China

[a] Authors to whom correspondence should be addressed: SunZX@sust.edu.cn; z.x.sun@utwente.nl; jhmei.dengdai@snnu.edu.cn; and puyongping@sust.edu.cn

ABSTRACT

Dielectric capacitors own great potential in next-generation energy storage devices for their fast charge-discharge time, while low energy storage capacity limits their commercialization. Enormous lead-free ferroelectric ceramic capacitor systems have been reported in recent decades, and energy storage density has increased rapidly. By comparing with some ceramic systems with fashioned materials or techniques, which lacks repeatability, as reported latterly, we proposed a unique but straightforward way to boost the energy storage capacity in a modified conventional ferroelectric system. Through stoichiometric ratio regulation, the coexistence of the C-phase and T-phase was obtained in 0.85 $(Ba_{1-x}Ca_x)(Zr_yTi_{1-y})O_3$-0.15BiSmO$_3$-2 wt. % MnO ceramics with $x = 0.1$ and $y = 0.15$ under the proof of the combination of *Rietveld* XRD refinement and transmission electron microscope measurement. The W_{rec} of 3.90 J/cm^3, an excellent value for BCZT-based ceramic at the present stage, was obtained because of the co-contribution of the optimization of electric field distribution and the additional interfacial polarization triggered at the higher electric fields. The finite element simulation and physical deduction, which fits very well with our experimental result, were also performed. As to the practical application, stable performance in a long-time cycle and frequency stability was obtained, and excellent discharge behaviors were also achieved.

Published under an exclusive license by AIP Publishing. https://doi.org/10.1063/5.0156119

Dielectric energy storage capacitors show great potential in modern electronic products, such as power systems due to their microsecond-level ultrafast charge–discharge time and megawatt-level ultrahigh power density.[1–5] However, by comparing with chemical energy storage devices, such as Li batteries and fuel cells, their energy storage capacity is relatively small, which hinders their miniaturization

and integration development in cutting-edge technologies.[6] Therefore, developing dielectric energy storage capacitors with high energy storage capacity and fast charge-discharge speed is becoming increasingly urgent. Typical lead-based ferroelectric materials, such as $PbLaZrTiO_3$-based systems, show great potential in energy storage capacitors. At the same time, the harm of Pb to both human-being and the environment will inevitably limit their applications,[7,8] leaving the chance for the development of lead-free ferroelectric systems. The energy storage capacity of a dielectric capacitor under a specific applied electrical field (E) can be represented by the following formula:[9]

$$W_{rec} = \int_{P_r}^{P_m} E dP. \tag{1}$$

where P is the generated polarization under E as well as P_m and P_r are the maximum polarization upon charging and the residual polarization when the electrical field returns to zero, respectively. Hence, to achieve a high energy storage density (W_{rec}), it is necessary to have both a high dielectric breakdown strength (E_b) and a large (P_m–P_r). In this case, most strategies are usually focused on two aspects: (1) fabricating relaxor ferroelectrics with both large-spontaneous-polarization and small domain size to achieve high (P_m–P_r);[10,11] (2) optimizing the preparation technology and refining the grain size to improve the E_b.[12]

After decades of exploration, lead-free energy storage ceramic now owns enormous systems like NBT-based,[13] KNN-based,[14] and $BiFeO_3$-based[15] systems, which significantly widen the application area of dielectric energy storage capacitors. Recently, $AgNbO_3$-based[16] antiferroelectrics and high entropy[17,18] relaxor ferroelectrics have attracted much attention. Though the W_{rec} has reached as high as 6.5[19] and 10.06 J/cm^3,[20] the difference in crystallization temperature of the former one and the high cost of the raw materials of the latter one make them far from commercial application. $BaTiO_3$-$BiMeO_3$ (BT-$BiMeO_3$)[21] is an excellent relaxor ferroelectric system with both large (P_m–P_r) and small coercive field (E_c), where the Me can be a single trivalent cation or two cations with an average of +3. It has been extensively studied due to its high energy efficiency (η) and W_{rec}. Yuan et al.[22] introduced $Bi(Zn_{0.5}Zr_{0.5})O_3$ into BT ceramics, and the W_{rec} of the ceramics reached 2.46 J/cm^3 due to the formation of nano-sized ferroelectric domains. Li et al.[23] reported that a high W_{rec} of 2.032 J/cm^3 and η of ~88% at 270 kV/cm could be obtained in $0.88BaTiO_3$-$0.12Bi(Li_{0.5}Nb_{0.5})O_3$ ceramics through component regulation. A high W_{rec} of 2.41 J/cm^3 and an excellent η as high as ~91.6% at 280 kV/cm were achieved in $0.85BaTiO_3$-$0.15Bi(Zn_{1/2}Sn_{1/2})O_3$ ceramics[24] that accompany with a good power density of 30.3 MW/cm^3 because of the disruption of long-range ordered ferroelectric domains. The majority of research on such systems only focuses on optimizing the $BiMeO_3$. At the same time, little work has been done to improve the contribution of BT, which is the more important ingredient in BT-$BiMeO_3$ systems. As a good solid solution of BT, $(Ba_{1-x}Ca_x)(Zr_yTi_{1-y})O_3$ (BCZT) shows typical relaxor ferroelectric behaviors due to its compositional fluctuation. In addition, it also exhibits high voltage endurance at its morphology phase boundary (MPB) for the optimization of electric field distribution,[25,26] which offers excellent potential in high-energy storage capacitors. Motivated by this, we chose BCZT instead of BT as our basis material, and $BiSmO_3$ was added for the high bandgap of Sm.[27] Meanwhile, MnO was doped to introduce defect dipoles for

P_m's further increasing[28] and $0.85(Ba_{1-x}Ca_x)(Zr_yTi_{1-y})O_3$-$0.15BiSmO_3$-2 wt. % MnO (BCZT-SM) ceramics were finally prepared via the solid-state method. Considering the significant effects of lattice parameters on the ferroelectric properties, we modulate the BCZT basis material by changing the Ca^{2+}/Zr^{2+} ratio to control the lattice parameters, and interestingly, the coexistence of tetragonal (T) phase and cubic(C) phase was also observed with $x = 0.1$ and $y = 0.15$, which shows a competitive W_{rec} among BCZT-based systems at this stage. This work revealed a fancy but easy way to improve the energy storage density in lead-free ceramics and offer a solid theoretical basis for optimizing functional materials.

Room-temperature XRD patterns of the BCZT-SM ceramics with different stoichiometric ratios ($x = 0.05$ and 0.10, $y = 0.1$ and 0.15), which abbreviate as BC5Z10T-SM, BC10Z10T-SM, BC5Z15T-SM, and BC10Z15T-SM, are shown in Fig. 1(a1). All the ceramics show pure perovskite structure, suggesting the dissolution of $BiSmO_3$ and MnO into the BCZT lattice. Figure 1(a2) depicts a local magnification around 45° to show the peak splitting at (002)/(200), which indicates the presence of T-phase in all the ceramics. In addition, an apparent lattice parameter variation can be judged by the peak shift according to the Bragg equation:[29–31]

$$2d \sin \theta = n\lambda, \tag{2}$$

where n, d, λ, and θ are an integer multiple of the wavelength, the spacing between parallel atomic planes, the incident wave wavelength, and the angle between the incident light and the crystal plane, respectively. The XRD data were driven by Rietveld refinement using the Fullprof for deeper analysis, and the results are displayed in Figs. 1 (b1)–1(b4), and some details of the refinement process are seen in the supplementary material. Interestingly, only T-phase exists in BC5Z10T-SM, BC10Z10T-SM, and BC5Z15T-SM, while the coexistence of both T and C-phases with a ratio of 54.16%/45.84% is detected in BC10Z15T-SM, and the ball-stick model of each phase was inserted in each figure. Figure 1(c) illustrates the Gaussian–Lorentz fitting result around 45° of XRD patterns of BC10Z15T-SM. The red scatter symbols are the experimental data, and the black lines are the fitted curve, which consists of two summed components. The yellow peak splits into two and represents the T-phase, and the blue one, which shows a single peak, represents the C-phase, which has a smaller out-of-plane lattice parameter (c).

Figures S1(a)–S1(d) display the scanning electron microscope (SEM) images of the top surface of these four ceramics. Though only a slight change in grain size is observed with component variation, BC10Z15T-SM exhibits a much better density and lower porosity than the others according to the morphology, which predicts a high electrical breakdown endurance. The corresponding energy dispersive x-ray spectroscopy (EDS) elemental mappings of are shown in Figs. 1(d1)–1 (d4). Ba, O, Mn, and Sm elements disperse uniformly in BC10Z15T-SM and can be confirmed through Ba-L, O-K, Mn-K, and Sm-L mappings, respectively. Transmission electron microscope (TEM) images of the BC10Z15T-SM are shown in Figs. S1(e) and S1(f), and the ferroelectric domains with different orientations can be seen in the areas marked with white dashed lines, which demonstrates the diffusion of the normal-sized ferroelectric domain in polar nanoregions (PNRs). Figure 2(a1) shows the atom-resolved high-angle annular dark field scanning transmission electron microscope (HAADF-STEM) image of BC10Z15T-SM ceramic. Since the local polarization in the ABO_3
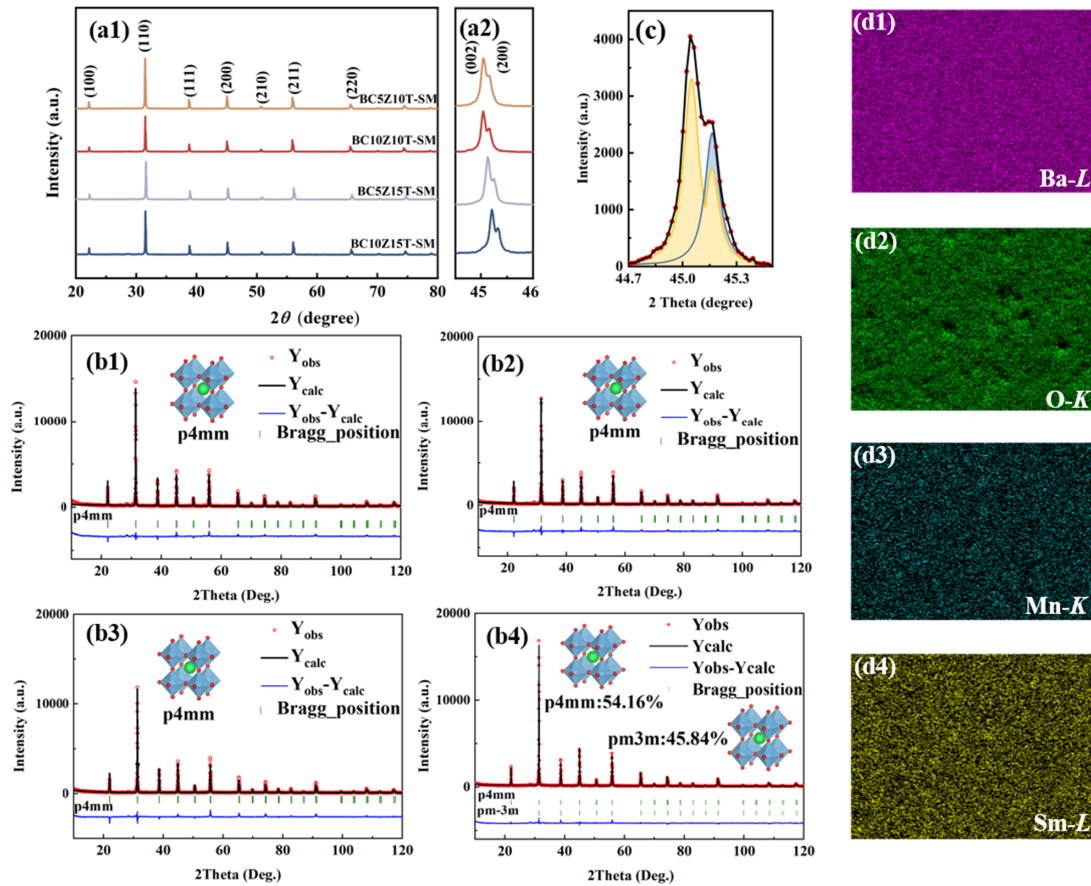
FIG. 1. (a1) XRD patterns of BCZT-SM in the 2θ range of $20°–80°$; (a2) enlarged view of (a1) from $44.5°–46°$; (b1)–(b4) Rietveld refinement of BCZT-SM; (c) the Gaussian–Lorentz fitting around $45°$ of BC10Z15T-SM; (d1)–(d4) SEM EDS mappings of the BC10Z15T-SM.

lattice can be determined by the displacement of the B-site cation concerning the nearest four A-site cation center,[30–32] polar regions can be observed according to the Ti-displacement or Zr-displacement in this work. Figures 2(a2)–2(a5) are the enlarged views of areas *1–4* of Fig. 2 (a1), and the spontaneous polarization orientation can be judged by the arrows. Areas *1* and *4* and areas *2* and *3* belong to the *C*-phase and *T*-phase, respectively. Figure 2(b1) shows the fast Fourier transform (FFT) image of BC10Z15T-SM, and the well-arranged patterns, which correspond to different lattice planes, can be observed. Figure 2(b2) is the enlarged view of the (101) plane of the FFT image, in which two patterns with close in-plane lattice parameters (*a*) but distinct *c*, which correspond to the *T*-phase and *C*-phase, can be seen. In Fig. 2(b3), with the FFT image of a higher angle of (301) plane, the value difference of *a* can be recognized by the included angle of θ. Figures 2(c2)–2 (c4) illustrate the atomic-EDS mappings of Ba-*L*, Ti-*L,* and Sm-*L* of the HAADF-STEM image from BC10Z15T-SM shown in Fig. 2(c1). The precise atom arrangement of Ba in the A-site can be seen in Fig. 2 (c2). Due to our sample's poor conductivity, the slice's ion-milled area kept jiggling under the hit of the electron beam without staying stable during the measurement. Not enough signals for forming the atomic EDS mappings can be collected. Despite this, we can still see the B-site

substitution of Ti and both A- and B-site substitution of Sm according to the position of the bright spots in Figs. 2(c3) and 2(c4). The TEM observations are consistent with the results of the two-phase coexistence in *Rietveld* refinement.

Figure S2 shows the temperature dependence of dielectric constant (ε) and dielectric loss (tanδ) of all these samples from $−160$ to $400\,°C$ at different frequencies with the fitting result of the *Curie-Weiss* law, and such ε-*T* and tanδ-*T* curves at 1 kHz are summarized in Fig. 3(a). The presence of *C*-phase in BC10Z15T-SM leads to its lowest ε and *tanδ*, but the best dielectric thermal stability, which is due to the limited displacement of Ti or Zr atom and shorter dipole moment.[33] The dielectric frequency stability of BC10Z15T-SM is also much better than the others, and a variation of the dielectric constant of only ~20 is obtained from 100 to 10^6 Hz, as seen in Fig. 3(b). Before W_{rec} calculation, the E_b of each ceramic should be confirmed based on the *Weibull* distribution as follows:[34,35]

$$X_i = \ln E_i, \tag{3}$$

$$Y_i = \ln(-\ln(1-P_i)), \tag{4}$$

$$P_i = \frac{i}{1+n}, \tag{5}$$
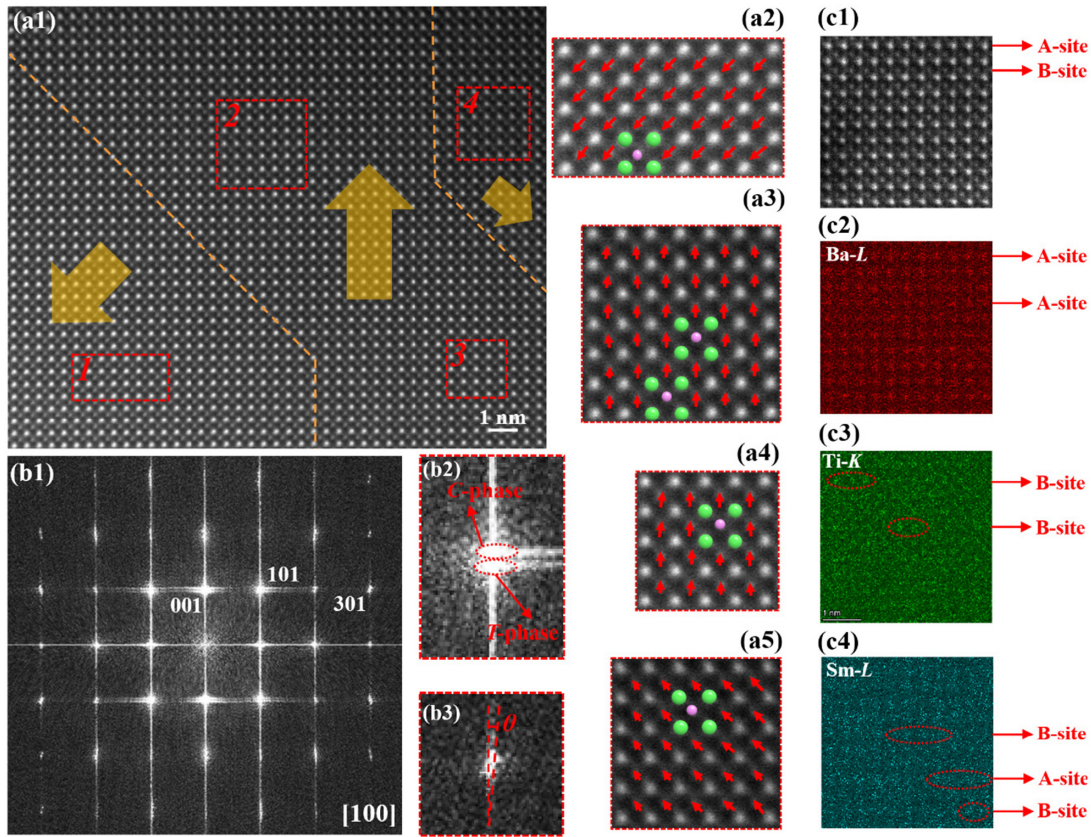
FIG. 2. (a1) Atom-resolved HAADF-STEM image of BC10Z15T-SM; (a2)–(a5) enlarged-view of area 1–4 in Fig. 2(a1); (b1) FFT image of BC10Z15T-SM; enlarged-view of (b2) (101) plane; (b3) (301) plane of Fig. 2(a1); (c1) HAADF-STEM image of BC10Z15T-SM is used for atomic-EDS mappings; atomic-EDS mappings of (c2) Ba-L; (c3) Ti-L; (c4) Sm-L, respectively, of 2 (c1).

where X_i and Y_i are the two parameters of the Weibull distribution, Y_i varies linearly with X_i with a slope of β, E_i and P_i are the sample's breakdown field and the electric field's failure probability distribution, respectively. However, n, i, and β are the total number of specimens, the serial number of dielectric strength, and the slope of the linear relationship between $\ln(E_i)$ and $\ln(-\ln(1-P_i))$, respectively. After calculating, the highest E_b of 335 kV/cm is located in BC10Z15T-SM, and the E_b of BC5Z10T-SM, BC10Z10T-SM, and BC5Z15T-SM is 270, 275, and 305 kV/cm, respectively, as displayed in Fig. 3(c). Figure 3(d) shows the unipolar hysteresis loops of all these ceramics performed at E_b under 100 Hz at room temperature, and the loop variations with electrical fields are shown in Figs. S3(a)–S3(d). All these ceramics exhibit super relaxor ferroelectric behavior with both higher P_m–P_r and lower E_c in a slim loop, which is a result of the addition of MnO in $0.85(Ba_{1-x}Ca_x)(Zr_yTi_{1-y})O_3$-$0.15BiSmO_3$, as explained in the supplementary material. The W_{rec} of BC5Z10T-SM, BC10Z10T-SM, BC5Z15T-SM, and BC10Z15T-SM was calculated to be 3.19, 2.53, 3.15, and 3.90 J/cm^3 by the integral of P with respect to E_m. The excellent performance of BC10Z15T-SM is attributed to the co-contribution of both the highest E_m and an optimistic polarization at a higher electrical field. The former is caused by the existence of the C-phase, which owns better high voltage endurance than the T-phase,

relying on its lower B-site atom displacement, as above-mentioned. The summary of the energy storage performance of BC10Z15T-SM is shown in Fig. S3(e).

To visually see the electric field redistribution, finite element simulation (FES) was carried out by driving the *COMSOL Multiphysics 5.6*. If we assume the adjacent T and C domains as capacitors with different ε connected in series, as sketched in Fig. S3(f), and due to the inversely proportional relationship between the ε and applied voltage (U) as we deduced in Eq. (S11), the mechanism of the electrical field distribution optimization can be revealed, as explained in the supplementary material. In this case, the electric potential in BC10Z15T-SM under high voltage becomes disordered, and the C-phase in BC10Z15T-SM attracts more voltage than T-phase, as seen in Figs. 4(a) and 4(b). By comparing with the others, the T-phase in BC10Z15T-SM suffers less partial voltage, and due to the better voltage endurance of the C-phase at the same time, BC10Z15T-SM, thus, shows the highest E_b. While just because of the existence of C-phase, the polarization of BC10Z15T-SM should also be lower than all the others because the polarization in a dielectric/ferroelectric material under a certain electrical field should have a positive correlation with both the dipole density and the dipole moment as we deduced Eq. (S18) in the supplementary material. The hysteresis loops, however,
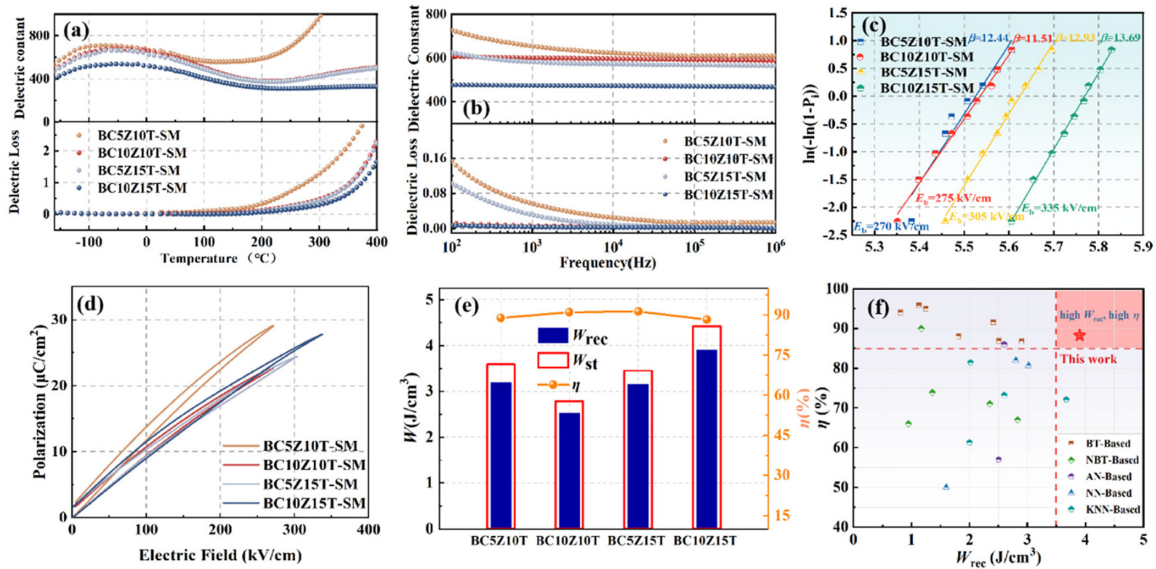
FIG. 3. (a) The temperature-dependent; (b) frequency-dependent of ε and tan δ; (c) the Weibull distribution for calculating the E_b of BCZT-SM; the unipolar P-E loops (d); the energy storage parameters (e) of BC10Z15T-SM measured at E_b/100 Hz at room temperature; (f) a comparison of the energy storage properties of BC10Z15T-SM with other reported dielectric energy-storage systems in the latest literature.
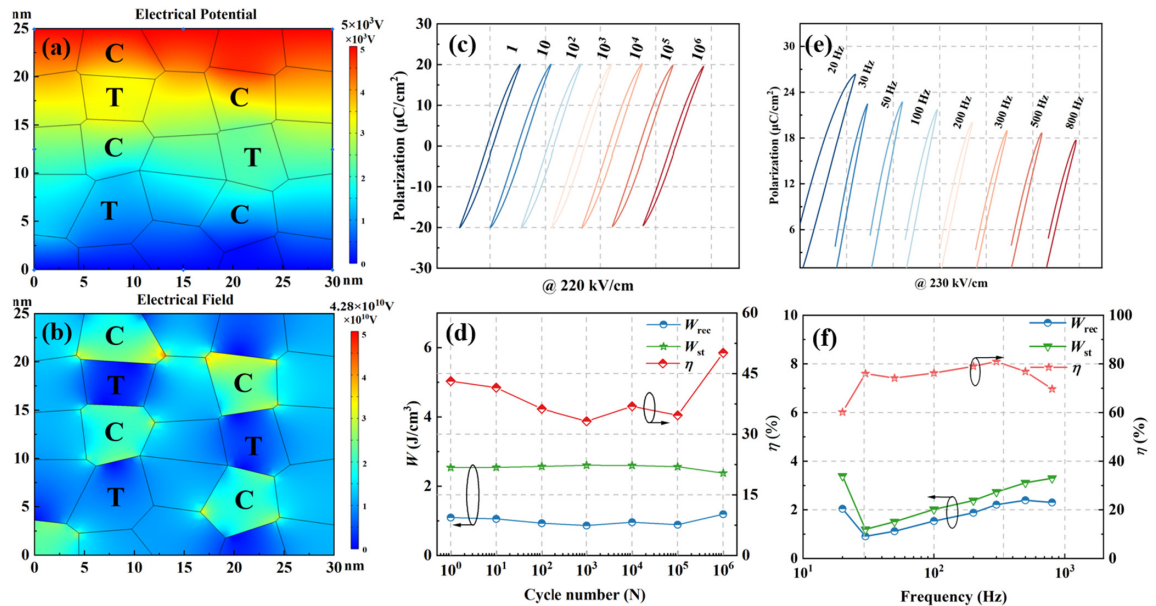
FIG. 4. (a) Electric potential distribution; (b) electric field distribution of the BC10Z15T-SM ceramic; (c) P-E loops; (d) energy storage parameters of BC10Z15T-SM ceramic at 220 kV/cm/100 Hz during 1 000 000 circles; (e) P-E loops; (f) energy storage parameters of BC10Z15T-SM ceramic at 230 kV/cm under the frequency range from 20 to 800 Hz.

show a different result as we expected that the polarization of BC10Z15T-SM is not the lowest under the electrical field from 0 to its E_b. This phenomenon is believed to be attributed to the interfacial polarization between T-phase and C-phase for their difference of ε,[36,37] and such an extra interfacial polarization can only be triggered when applying a higher voltage to the materials. That is why the

BC10Z15T-SM has the lowest ε value in both ε-T and ε-f curves but owns a much higher polarization in P-E loops. To clarify this, we extracted the P_m, W_{rec}, and η of all the ceramics under 260 kV/cm from Fig. S3 and plotted them in Fig. S4. The P_m of BC10Z15T-SM, which has the lowest ε, is higher than that in both BC10Z10T-SM and BC5Z15T-SM. The values of W_{rec}, W_{st}, and η for all these ceramics at
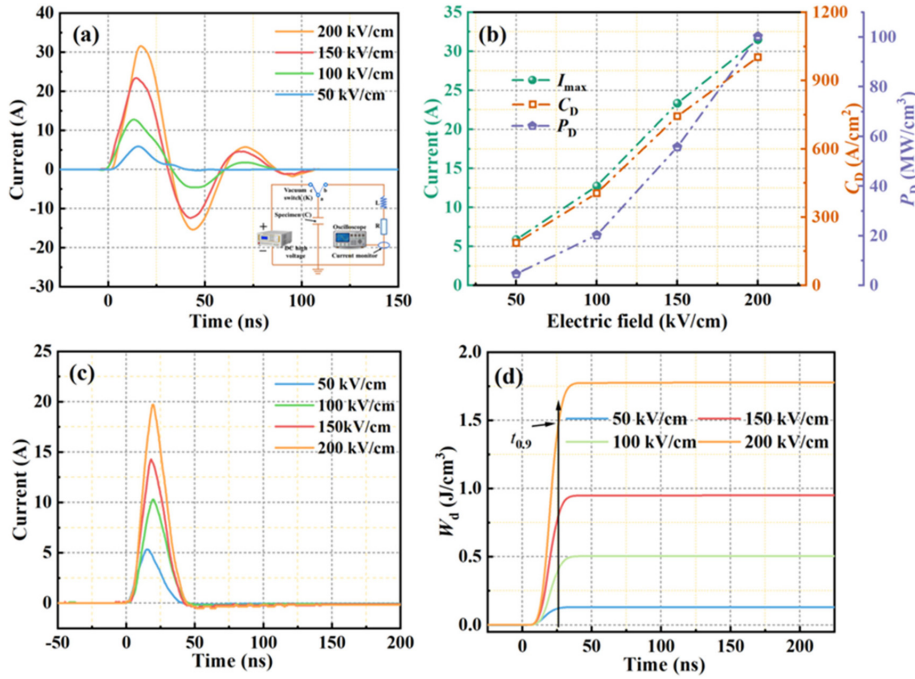
FIG. 5. Underdamped discharge waveforms (a); Imax, C_D, and P_D (b); overdamped discharge current curves (c); and W_d depending on time (d) of BC10Z15T-SM at different electrical fields. The equivalent circuit of this test is insetted in Fig. 5(a).

E_b were calculated and summarized in Fig. 3(e). The difference value of W_{rec} between the BCZT-SM ceramics with different stoichiometric ratios is as high as 1.37 J/cm^3, which means that an increment of 54.15% in W_{rec} was obtained by component regulation. Including this work, Fig. 3(f) summarizes the energy storage performance of other reported dielectric energy storage systems in the latest literature studies,[38–58] and it can be seen that the BC10Z15T-SM ceramics have outstanding advantages over others in terms of overall performance.

To characterize its reliability, the polarization fatigue and energy storage frequency stability of BC10Z15T-SM were tested. Figure 4(c) shows its bipolar hysteresis loop of under 220 kV/cm/100 Hz during 1 000 000 cycles, and the corresponding energy storage parameters are summarized in Fig. 4(d). The fluctuations of W_{rec}, W_{st}, and η with a variation of only 27%, 7.4%, and 33.7% were achieved, respectively, which matches well with the excellent dielectric frequency stability. Figure 4(e) depicts the unipolar P-E loops of the BC10Z15T-SM at the frequency range of 20–800 Hz under the electric field of 230 kV/cm, and the corresponding parameters are displayed in Fig. 4(f). The P_m decreases with increasing frequency because some relaxation polarizations cannot keep up with the switching of the applied electrical field, especially at higher voltages, which is consistent with the result in ε-f curves. Both the fatigue and frequency stability of energy storage indicate the reliability of BC10Z15T-SM. The practical application performance of the BC10Z15T-SM capacitor in terms of energy storage is evaluated using a pulsed charge-discharge test. The underdamped discharge curves of BC10Z15T-SM ceramic under different electrical fields are determined using an R-L-C circuit, as shown in Fig. 5(a). It can be seen that this capacitor exhibits highly similar discharge behaviors under different electric fields. As the electric field increases, the peak value of the first current also increases continuously, and I_{max} increases from 5.8 to 31.5 A. The variation of their current density C_D

and electric field density P_D is accounted for in Fig. 5(b), as two momentous parameters can be obtained by the following formulas:[59–62]

$$C_D = I_{max}/S, \tag{6}$$

$$P_D = EI_{max}/2S. \tag{7}$$

From the equation, the C_D and P_D keep the same trend as the peak current, achieving the values of 1003.18 A/cm^2 and 100.32 MW/cm^3 at 200 kV/cm, respectively. Figure 5(c) shows the overdamped pulse discharge current under different electric fields when the load resistance is 100 Ω. The peak current increases similarly, with E varying from 50 to 200 kV/cm. The time dependence of the discharge energy density [W_d, Fig. 5(d)] can be calculated from the overdamped discharge current curve using the formula:

$$W_d = R \int i^2(t)dt/V. \tag{8}$$

R is the load resistance, V is the sample volume, I is the discharge current, and t is time. Based on this, the large current is conducive to obtaining high W_d. As shown in Fig. 5(d), W_d increases from 0.130 J/cm^3 at 50 kV/cm^3 to 1.785 J/cm^3 at 200 kV/cm^3. Generally, the $t_{0.9}$ parameter is the time required for dielectric capacitors to release 90% of the total energy stored. It is apparent that the BC10Z15T-SM-SM ceramic exhibits a speedy and stable discharge rate with a $t_{0.9}$ of 26 ns. These results indicate that BC10Z15T-SM-SM ceramic is a promising candidate for pulsed power capacitor applications.

Via the regulation of stoichiometric ratio in 0.85(Ba$_{1-x}$Ca$_x$)(Zr$_y$Ti$_{1-y}$)O$_3$-0.15BiSmO$_3$-2 wt. % MnO ceramics fabricated through solid-state reaction, the lattice variation was observed in XRD result. By combining the *Rietveld* refinement with TEM, the co-existence of

T-phase and C-phase was obtained with $x = 0.1$ and $y = 0.15$, while the others contain only T-phase. Due to the co-contribution of optimization of electric field distribution and the extra interfacial polarization triggered at the higher electrical field, which is a result of the existence of C-phase, the W_{rec} of 3.90 J/cm^3, which is quite a competitive value for BCZT-based polycrystalline ceramic, was obtained. The finite element simulation and significant physical deduction were also performed, and both fit well with our experimental result. In addition, good ferroelectric fatigue and frequency stability of energy storage were also characterized, and a good discharge performance was obtained. Our work offers a unique but simple way to achieve high W_{rec} in ferroelectric capacitors.

See the supplementary material for the experimental procedure, some additional discussions, the mathematical derivation, and some additional figures.

AUTHOR DECLARATIONS
Conflict of Interest

The authors have no conflicts to disclose.

Author Contributions

Zixiong Sun: Conceptualization (equal); Project administration (equal); Writing – original draft (equal); Writing – review & editing (equal). **Ye Tian:** Writing – original draft (equal). **Yongping Pu:** Writing – review & editing (equal). **Yuhan Bai:** Data curation (equal). **Tao Ouyang:** Methodology (equal). **Qing Guo:** Data curation (equal). **Yating Ning:** Methodology (equal). **Jiaqi Liu:** Methodology (equal). **Hansong Wei:** Methodology (equal). **Kang Du:** Writing – review & editing (equal). **Hongmei Jing:** Data curation (equal).

DATA AVAILABILITY

The data that support the findings of this study are available from the corresponding authors upon reasonable request.

REFERENCES

[1] H. Palneedi, M. Peddigari, G.-T. Hwang, D.-Y. Jeong, and J. Ryu, "High-performance dielectric ceramic films for energy storage capacitors: Progress and outlook," Adv. Funct. Mater. **28**(42), 1803665 (2018).

[2] Z. Sun, Z. Wang, Y. Tian, G. Wang, W. Wang, M. Yang, X. Wang, F. Zhang, and Y. Pu, "Progress, outlook, and challenges in lead-free energy-storage ferroelectrics," Adv. Electron. Mater. **6**(1), 1900698 (2020).

[3] N. Luo, L. Ma, G. Luo, C. Xu, L. Rao, Z. Chen, Z. Cen, Q. Feng, X. Chen, F. Toyohisa, Y. Zhu, J. Hong, J.-F. Li, and S. Zhang, "Well-defined double hysteresis loop in NaNbO₃ antiferroelectrics," Nat. Commun. **14**(1), 1776 (2023).

[4] D. Li, X. Zeng, Z. Li, Z.-Y. Shen, H. Hao, W. Luo, X. Wang, F. Song, Z. Wang, and Y. Li, "Progress and perspectives in dielectric energy storage ceramics," J. Adv. Ceram. **10**(4), 675–703 (2021).

[5] Z. Sun, Y. Bai, J. Liu, G. Jian, C. Guo, L. Zhang, and Y. Pu, "Interface engineering in ferroelectrics: From films to bulks," J. Alloys Compd. **909**, 164735 (2022).

[6] M. R. Lukatskaya, B. Dunn, and Y. Gogotsi, "Multidimensional materials and device architectures for future hybrid energy storage," Nat. Commun. **7**(1), 12647 (2016).

[7] G. H. Haertling, "PLZT electrooptic materials and applications–A review," Ferroelectrics **75**(1), 25–55 (1987).

[8] P. K. Panda and B. Sahoo, "PZT to lead free piezo ceramics: A review," Ferroelectrics **474**(1), 128–143 (2015).

[9] L. Ma, Z. Che, C. Xu, Z. Cen, Q. Feng, X. Chen, F. Toyohisa, J.-F. Li, S. Zhang, and N. Luo, "High energy storage density and efficiency in AgNbO₃ based relaxor antiferroelectrics with reduced silver content," J. Eur. Ceram. Soc. **43**(8), 3228–3235 (2023).

[10] P. Maksymovych, S. Jesse, P. Yu, R. Ramesh, A. P. Baddorf, and S. V. Kalinin, "Polarization control of electron tunneling into ferroelectric surfaces," Science **324**(5933), 1421–1425 (2009).

[11] H. Du, F. Tang, D. Liu, D. Zhu, W. Zhou, and S. Qu, "The microstructure and ferroelectric properties of (K₀.₅Na₀.₅)NbO₃–LiNbO₃ lead-free piezoelectric ceramics," Mater. Sci. Eng. B **136**(2), 165–169 (2007).

[12] T. Ouyang, Y. Pu, J. Ji, S. Zhou, and R. Li, "Ultrahigh energy storage capacity with superfast discharge rate achieved in Mg-modified Ca₀.₅Sr₀.₅TiO₃-based lead-free linear ceramics for dielectric capacitor applications," Ceram. Int. **47**(14), 20447–20455 (2021).

[13] O. Elkechai, M. Manier, and J. P. Mercurio, "Na₀.₅Bi₀.₅TiO₃–K₀.₅Bi₀.₅TiO₃ (NBT-KBT) system: A structural and electrical study," Phys. Status Solidi A **157**(2), 499–506 (1996).

[14] D. Li, D. Zhou, D. Wang, W. Zhao, Y. Guo, and Z. Shi, "Improved energy storage properties achieved in (K, Na) NbO₃-based relaxor ferroelectric ceramics via a combinatorial optimization strategy," Adv. Funct. Mater. **32**(15), 2111776 (2022).

[15] F. Chang, N. Zhang, F. Yang, S. Wang, and G. Song, "Effect of Cr substitution on the structure and electrical properties of BiFeO₃ ceramics," J. Phys. D: Appl. Phys. **40**(24), 7799 (2007).

[16] Z. Liu, T. Lu, J. M. Ye, G. S. Wang, X. L. Dong, R. Withers, and Y. Liu, "Antiferroelectrics for energy storage applications: A review," Adv. Mater. Technol. **3**, 1800111 (2018).

[17] Y. Ning, Y. Pu, C. Wu, S. Zhou, L. Zhang, J. Zhang, X. Zhang, and Y. Shang, "Enhanced capacitive energy storage and dielectric temperature stability of A-site disordered high-entropy perovskite oxides," J. Mater. Sci. Technol. **145**, 66–73 (2023).

[18] Y. Ning, Y. Pu, Q. Zhang, S. Zhou, C. Wu, L. Zhang, Y. Shi, and Z. Sun, "Achieving high energy storage properties in perovskite oxide via high-entropy design," Ceram. Int. **49**(8), 12214–12223 (2023).

[19] Z. Lu, W. Bao, G. Wang, S.-K. Sun, L. Li, J. Li, H. Yang, H. Ji, A. Feteira, D. Li, F. Xu, A. K. Kleppe, D. Wang, S.-Y. Liu, and I. M. Reaney, "Mechanism of enhanced energy storage density in AgNbO₃-based lead-free antiferroelectrics," Nano Energy **79**, 105423 (2021).

[20] L. Chen, S. Deng, H. Liu, J. Wu, H. Qi, and J. Chen, "Giant energy-storage density with ultrahigh efficiency in lead-free relaxors via high-entropy design," Nat. Commun. **13**(1), 3089 (2022).

[21] M. A. Beuerlein, N. Kumar, T.-M. Usher, H. J. Brown-Shaklee, N. Raengthon, I. M. Reaney, D. P. Cann, J. L. Jones, and G. L. Brennecka, "Current understanding of structure–processing–property relationships in BaTiO₃–Bi(M)O₃ dielectrics," J. Am. Ceram. Soc. **99**(9), 2849–2870 (2016).

[22] Q. Yuan, F. Yao, Y. Wang, R. Ma, and H. Wang, "Relaxor ferroelectric 0.9BaTiO₃–0.1Bi(Zn₀.₅Zr₀.₅)O₃ ceramic capacitors with high energy density and temperature stable energy storage properties," J. Mater. Chem. C **5**(37), 9552–9558 (2017).

[23] W.-B. Li, D. Zhou, L.-X. Pang, R. Xu, and H.-H. Guo, "Novel barium titanate based capacitors with high energy density and fast discharge performance," J. Mater. Chem. A **5**(37), 19607–19612 (2017).

[24] M. Zhou, R. Liang, Z. Zhou, and X. Dong, "Novel BaTiO₃-based lead-free ceramic capacitors featuring high energy storage density, high power density, and excellent stability," J. Mater. Chem. C **6**(31), 8528–8537 (2018).

[25] Y. Bai, A. Matousek, P. Tofel, V. Bijalwan, B. Nan, H. Hughes, and T. W. Button, "(Ba, Ca)(Zr, Ti) O₃ lead-free piezoelectric ceramics—The critical role of processing on properties," J. Eur. Ceram. Soc. **35**(13), 3445–3456 (2015).

[26]Z. Hanani, D. Mezzane, M. Amjoud, S. Fourcade, A. G. Razumnaya, I. A. Luk'Yanchuk, and M. Gouné, "Enhancement of dielectric properties of lead-free BCZT ferroelectric ceramics by grain size engineering," Superlattices Microstruct. **127**, 109–117 (2019).

[27]A. Kumari, K. Kumari, F. Ahmed, A. Alshoaibi, P. A. Alvi, S. Dalela, M. M. Ahmad, R. N. Aljawfi, P. Dua, A. Vij, and S. Kumar, "Influence of Sm doping on structural, ferroelectric, electrical, optical and magnetic properties of $BaTiO_3$," Vacuum **184**, 109872 (2021).

[28]P. Parjansri and S. Eitssayeam, "Effects of MnO_2 doping on the electrical properties of BCZT ceramics prepared by seed-induced method," Ferroelectrics **534**(1), 63–70 (2018).

[29]C. G. Pope, "X-ray diffraction and the Bragg equation," J. Chem. Educ. **74**(1), 129 (1997).

[30]Y. Ivry, D. P. Chu, J. F. Scott, and C. Durkan, "Flux closure vortexlike domain structures in ferroelectric thin films," Phys. Rev. Lett. **104**(20), 207602 (2010).

[31]N. Balke, P. Maksymovych, S. Jesse, A. Herklotz, A. Tselev, C.-B. Eom, I. I. Kravchenko, P. Yu, and S. V. Kalinin, "Differentiating ferroelectric and nonferroelectric electromechanical effects with scanning probe microscopy," ACS Nano **9**(6), 6484–6492 (2015).

[32]M. Ghita, M. Fornari, D. J. Singh, and S. V. Halilov, "Interplay between A-site and B-site driven instabilities in perovskites," Phys. Rev. B **72**(5), 054114 (2005).

[33]Z.-X. Chen, Y. Chen, and Y.-S. Jiang, "DFT study on ferroelectricity of $BaTiO_3$," J. Phys. Chem. B **105**(24), 5766–5771 (2001).

[34]Y. Huan, T. Wei, X. Wang, X. Liu, P. Zhao, and X. Wang, "Achieving ultrahigh energy storage efficiency in local-composition gradient-structured ferroelectric ceramics," Chem. Eng. J. **425**, 129506 (2021).

[35]L. Liu, Y. Liu, J. Hao, J. Chen, P. Li, S. Chen, P. Fu, W. Li, and J. Zhai, "Multi-scale collaborative optimization of $SrTiO_3$-based energy storage ceramics with high performance and excellent stability," Nano Energy **109**, 108275 (2023).

[36]M. P. Kim, D.-S. Um, Y.-E. Shin, and H. Ko, "High-performance triboelectric devices via dielectric polarization: A review," Nanoscale Res. Lett. **16**, 1–14 (2021).

[37]X. Xie, C. Yang, X. Qi, J. Yang, Z. Zhou, and Y. Wang, "Constructing polymeric interlayer toward high dielectric constant and low dielectric loss," Chem. Eng. J. **366**, 378–389 (2019).

[38]Q. Xu, H. Liu, Z. Song, X. Huang, A. Ullah, L. Zhang, J. Xie, H. Hao, M. Cao, and Z. Yao, "A new energy-storage ceramic system based on $Bi_{0.5}Na_{0.5}TiO_3$ ternary solid solution," J. Mater. Sci.: Mater. Electron. **27**(1), 322–329 (2016).

[39]A. Xie, H. Qi, and R. Zuo, "Achieving remarkable amplification of energy-storage density in two-step sintered $NaNbO_3$–$SrTiO_3$ antiferroelectric capacitors through dual adjustment of local heterogeneity and grain scale," ACS Appl. Mater. Interfaces **12**(17), 19467–19475 (2020).

[40]Q. Hu, L. Jin, T. Wang, C. Li, Z. Xing, and X. Wei, "Dielectric and temperature stable energy storage properties of $0.88BaTiO_3$–$0.12Bi(Mg_{1/2}Ti_{1/2})O_3$ bulk ceramics," J. Alloys Compd. **640**, 416–420 (2015).

[41]Y. Yao, Y. Li, N. Sun, J. Du, X. Li, L. Zhang, Q. Zhang, and X. Hao, "Enhanced dielectric and energy-storage properties in ZnO-doped $0.9(0.94Na_{0.5}Bi_{0.5}TiO_3-0.06BaTiO_3)-0.1NaNbO_3$ ceramics," Ceram. Int. **44**(6), 5961–5966 (2018).

[42]B. Qu, H. Du, Z. Yang, Q. Liu, and T. Liu, "Enhanced dielectric breakdown strength and energy storage density in lead-free relaxor ferroelectric ceramics prepared using transition liquid phase sintering," RSC Adv. **6**(41), 34381–34389 (2016).

[43]X. Jiang, H. Hao, S. Zhang, J. Lv, M. Cao, Z. Yao, and H. Liu, "Enhanced energy storage and fast discharge properties of $BaTiO_3$ based ceramics modified by $Bi(Mg_{1/2}Zr_{1/2})O_3$," J. Eur. Ceram. Soc. **39**(4), 1103–1109 (2019).

[44]Z. Liu, P. Ren, C. Long, X. Wang, Y. Wan, and G. Zhao, "Enhanced energy storage properties of $NaNbO_3$ and $SrZrO_3$ modified $Bi_{0.5}Na_{0.5}TiO_3$ based ceramics," J. Alloys Compd. **721**, 538–544 (2017).

[45]Y. Lin, D. Li, M. Zhang, S. Zhan, Y. Yang, H. Yang, and Q. Yuan, "Excellent energy-storage properties achieved in $BaTiO_3$-based lead-free relaxor ferroelectric ceramics via domain engineering on the nanoscale," ACS Appl. Mater. Interfaces **11**(40), 36824–36830 (2019).

[46]H. Qi, R. Zuo, A. Xie, J. Fu, and D. Zhang, "Excellent energy-storage properties of $NaNbO_3$-based lead-free antiferroelectric orthorhombic P-phase (Pbma) ceramics with repeatable double polarization-field loops," J. Eur. Ceram. Soc. **39**(13), 3703–3709 (2019).

[47]R. M. Pallares, X. Su, S. H. Lim, and N. T. K. Thanh, "Fine-tuning of gold nanorod dimensions and plasmonic properties using the Hofmeister effects," J. Mater. Chem. C **4**(1), 53–61 (2016).

[48]Z. Yang, F. Gao, H. Du, L. Jin, L. Yan, Q. Hu, Y. Yu, S. Qu, X. Wei, Z. Xu, and Y.-J. Wang, "Grain size engineered lead-free ceramics with both large energy storage density and ultrahigh mechanical properties," Nano Energy **58**, 768–777 (2019).

[49]Y. Pu, L. Zhang, Y. Cui, and M. Chen, "High energy storage density and optical transparency of microwave sintered homogeneous $(Na_{0.5}Bi_{0.5})_{(1-x)}Ba_xTi_{(1-y)}Sn_yO_3$ ceramics," ACS Sustainable Chem. Eng. **6**(5), 6102–6109 (2018).

[50]X. Zhao, Z. Zhou, R. Liang, F. Liu, and X. Dong, "High-energy storage performance in lead-free $(1-x)BaTiO_3$-$xBi(Zn_{0.5}Ti_{0.5})O_3$ relaxor ceramics for temperature stability applications," Ceram. Int. **43**(12), 9060–9066 (2017).

[51]X. Zhou, H. Qi, Z. Yan, G. Xue, H. Luo, and D. Zhang, "Large energy density with excellent stability in fine-grained $(Bi_{0.5}Na_{0.5})TiO_3$-based lead-free ceramics," J. Eur. Ceram. Soc. **39**(14), 4053–4059 (2019).

[52]L. Zhao, Q. Liu, S. Zhang, and J.-F. Li, "Lead-free $AgNbO_3$ anti-ferroelectric ceramics with an enhanced energy storage performance using MnO_2 modification," J. Mater. Chem. C **4**(36), 8380–8384 (2016).

[53]B. Qu, H. Du, and Z. Yang, "Lead-free relaxor ferroelectric ceramics with high optical transparency and energy storage ability," J. Mater. Chem. C **4**(9), 1795–1803 (2016).

[54]M. Zhou, R. Liang, Z. Zhou, S. Yan, and X. Dong, "Novel sodium niobate-based lead-free ceramics as new environment-friendly energy storage materials with high energy density, high power density, and excellent stability," ACS Sustainable Chem. Eng. **6**(10), 12755–12765 (2018).

[55]Y. Tian, L. Jin, H. Zhang, Z. Xu, X. Wei, G. Viola, I. Abrahams, and H. Yan, "Phase transitions in bismuth-modified silver niobate ceramics for high power energy storage," J. Mater. Chem. A **5**(33), 17525–17531 (2017).

[56]T. Wang, L. Jin, C. Li, Q. Hu, and X. Wei, "Relaxor ferroelectric $BaTiO_3$-$Bi(Mg_{2/3}Nb_{1/3})O_3$ ceramics for energy storage application," J. Am. Ceram. Soc. **98**(2), 559–566 (2015).

[57]Z. Yang, H. Du, S. Qu, Y. Hou, H. Ma, J. Wang, J. Wang, X. Wei, and Z. Xu, "Significantly enhanced recoverable energy storage density in potassium–sodium niobate-based lead free ceramics," J. Mater. Chem. A **4**(36), 13778–13785 (2016).

[58]Q. Yuan, G. Li, F.-Z. Yao, S.-D. Cheng, Y. Wang, R. Ma, S.-B. Mi, M. Gu, K. Wang, J.-F. Li, and H. Wang, "Simultaneously achieved temperature-insensitive high energy density and efficiency in domain engineered $BaTiO_3$-$Bi(Mg_{0.5}Zr_{0.5})O_3$ lead-free relaxor ferroelectrics," Nano Energy **52**, 203–210 (2018).

[59]Y. Li, Y. Liu, M. Tang, J. Lv, F. Chen, Q. Li, Y. Yan, F. Wu, L. Jin, and G. Liu, "Energy storage performance of $BaTiO_3$-based relaxor ferroelectric ceramics prepared through a two-step process," Chem. Eng. J. **419**, 129673 (2021).

[60]D. Wang, Z. Fan, W. Li, D. Zhou, A. Feteira, G. Wang, S. Murakami, S. Sun, Q. Zhao, X. Tan, and I. M. Reaney, "High energy storage density and large strain in $Bi(Zn_{2/3}Nb_{1/3})O_3$-doped $BiFeO_3$–$BaTiO_3$ ceramics," ACS Appl. Energy Mater. **1**(8), 4403–4412 (2018).

[61]J. Ma, D. Zhang, F. Ying, X. Li, L. Li, S. Guo, Y. Huan, J. Zhang, J. Wang, and S.-T. Zhang, "Ultrahigh energy storage density and high efficiency in lead-free $(Bi_{0.9}Na_{0.1})(Fe_{0.8}Ti_{0.2})O_3$-modified $NaNbO_3$ ceramics via stabilizing the antiferroelectric phase and enhancing relaxor behavior," ACS Appl. Mater. Interfaces **14**(17), 19704–19713 (2022).

[62]C. Li, J. Liu, L. Lin, W. Bai, S. Wu, P. Zheng, J. Zhang, and J. Zhai, "Superior energy storage capability and stability in lead-free relaxors for dielectric capacitors utilizing nanoscale polarization heterogeneous regions," Small **19**(12), 2206662 (2023).